THE JOURNAL OF BIOLOGICAL CHEMISTRY VOL. 292, NO. 5, pp. 1749–1761, February 3, 2017

Structure of the Lipid Nanodisc-reconstituted Vacuolar ATPase Proton Channel

*DEFINITION OF THE INTERACTION OF ROTOR AND STATOR AND IMPLICATIONS FOR ENZYME REGULATION BY REVERSIBLE DISSOCIATION**

Received for publication, November 8, 2016, and in revised form, December 11, 2016 Published, JBC Papers in Press, December 13, 2016, DOI 10.1074/jbc.M116.766790

Nicholas J. Stam and Stephan Wilkens[1]

From the Department of Biochemistry and Molecular Biology, State University of New York Upstate Medical University, Syracuse, New York 13210

Edited by Norma Allewell

Eukaryotic vacuolar H^+-ATPase (V-ATPase) is a multisubunit enzyme complex that acidifies subcellular organelles and the extracellular space. V-ATPase consists of soluble V_1-ATPase and membrane-integral V_o proton channel sectors. To investigate the mechanism of V-ATPase regulation by reversible disassembly, we recently determined a cryo-EM reconstruction of yeast V_o. The structure indicated that, when V_1 is released from V_o, the N-terminal cytoplasmic domain of subunit *a* (a_{NT}) changes conformation to bind rotor subunit *d*. However, insufficient resolution precluded a precise definition of the a_{NT}-*d* interface. Here we reconstituted V_o into lipid nanodiscs for single-particle EM. 3D reconstructions calculated at ~15-Å resolution revealed two sites of contact between a_{NT} and *d* that are mediated by highly conserved charged residues. Alanine mutagenesis of some of these residues disrupted the a_{NT}-*d* interaction, as shown by isothermal titration calorimetry and gel filtration of recombinant subunits. A recent cryo-EM study of holo V-ATPase revealed three major conformations corresponding to three rotational states of the central rotor of the enzyme. Comparison of the three V-ATPase conformations with the structure of nanodisc-bound V_o revealed that V_o is halted in rotational state 3. Combined with our prior work that showed autoinhibited V_1-ATPase to be arrested in state 2, we propose a model in which the conformational mismatch between free V_1 and V_o functions to prevent unintended reassembly of holo V-ATPase when activity is not needed.

The vacuolar H^+-ATPase (V-ATPase,[2] V_1V_o-ATPase) is a large multisubunit enzyme complex found in the endomembrane system of all eukaryotic cells, where it acidifies the lumen of subcellular organelles, including lysosomes, endosomes, the Golgi apparatus, and clathrin-coated vesicles (1–4). V-ATPase function is essential for pH and ion homeostasis (2), protein trafficking, endocytosis, mechanistic target of rapamycin (mTOR) (5, 6), and Notch (7) signaling as well as hormone secretion (8) and neurotransmitter release (9). In animals, V-ATPase can also be found in the plasma membrane of polarized cells, where its proton pumping function is involved in bone remodeling, urine acidification, and sperm maturation (1). The essential nature of eukaryotic V-ATPase is highlighted by the fact that complete loss of V-ATPase activity in animals is embryonic lethal (10). On the other hand, partial loss of enzyme function (or hyperactivity) has been associated with numerous widespread human diseases, including, but not limited to, renal tubular acidosis (11), osteoporosis (12), neurodegeneration (13), male infertility (14), deafness (15), diabetes (8), and cancer (16). Furthermore, V-ATPase is targeted by pathogens such as *Mycobacterium tuberculosis* or *Legionella pneumophila* (17, 18) to facilitate pathogen entry and survival. Because of its essential nature and key role in so many human diseases, V-ATPase has been identified as a potential drug target (19–21).

V-ATPase can be divided into a soluble catalytic sector, V_1, and a membrane-integral proton channel sector, V_o (Fig. 1). In the yeast *Saccharomyces cerevisiae*, V_1 is composed of eight different polypeptides, AB(C)DEFGH, that are arranged in an A_3B_3 catalytic hexamer with a central stalk made of DF and three peripheral stators (EG heterodimers), one of which binds the single-copy H subunit. The ~320-kDa V_o contains subunits *acc'c"de*, which are organized in a membrane-integral "proteolipid" ring ($c_8c'c"$ (22, 23)), a membrane-bound subunit *a* with an integral C-terminal domain (a_{CT}) that is bound at the periphery of the proteolipid ring, and an N-terminal cytoplasmic domain (a_{NT}) that is bound to subunit *d* (Fig. 1). The stoichiometry, location, and function of subunit *e* are not known. Eukaryotic V-ATPase belongs to the family of energy-transducing rotary motor ion pumps that also includes F_1F_o-ATP synthase, archaeal A-ATPase, and bacterial A/V-like ATPase (24, 25). In V-ATPase, ATP hydrolysis at three catalytic sites in the A_3B_3 hexamer is coupled to proton translocation via rotation of V_1 subunits DF that are connected to the subunit *d*-proteolipid ring subcomplex of V_o. Proton translocation is through two aqueous half-channels at the interface of a_{CT} and the prote-

* This work was supported by National Institutes of Health Grant GM058600 (to S. W.). The authors declare that they have no conflicts of interest with the contents of this article. The content is solely the responsibility of the authors and does not necessarily represent the official views of the National Institutes of Health.

The 3D EM reconstructions of V_oND and V_oND-CaM have been deposited in the EMDB with accession numbers EMD-6335 and EMD-6336, respectively.

[1] To whom correspondence should be addressed: Dept. of Biochemistry and Molecular Biology, SUNY Upstate Medical University, 750 E. Adams St., Syracuse, NY 13210. Tel.: 315-464-8703; E-mail: wilkenss@upstate.edu.

[2] The abbreviations used are: V-ATPase, vacuolar ATPase; V_o, membrane sector of the vacuolar ATPase; V_oND, membrane sector of the vacuolar ATPase reconstituted in lipid nanodiscs; a_{NT}, N-terminal cytoplasmic domain of the *a* subunit; CaM, calmodulin; FSC, Fourier shell correlation; ITC, isothermal titration calorimetry; MBP, maltose binding protein; UnDM, undecyl-β-D-maltoside; MSP, MSP1E3D1; TCEP, tris(2-carboxyethyl)phosphine.

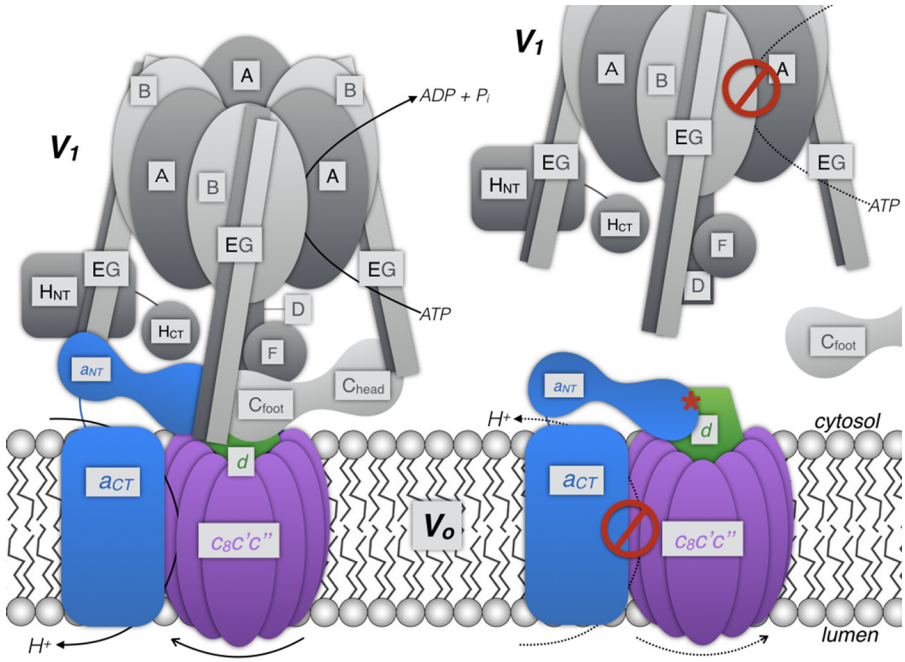

FIGURE 1. **Schematic of V-ATPase architecture and the mechanism of regulation by reversible disassembly.** V_1 is represented by subunits shaded in *gray*. Subunits of V_o are shown in *blue* (*a*), *purple* (*c*-ring composed of $c_8c'c''$), and *green* (*d*). ATP hydrolysis in V_1 drives rotation of the *c*-ring, resulting in proton translocation across the interface of the *c*-ring and a_{CT}. Upon reversible disassembly, subunit C is released into the cytoplasm, and the interactions between subunits of V_1 (DF and EG1–3) and V_o (a_{NT}, *d*) are broken. Disassembly of the enzyme results in a V_1 that does not hydrolyze MgATP and a V_o that does not support passive proton translocation. Note that, upon release of V_1 from the membrane, a_{NT} changes conformation to bind the central rotor subunit *d* (*red asterisk*) as reported previously (38).

olipid ring and involves membrane-embedded essential glutamate and arginine residues in the *c* subunits and a_{CT}, respectively.

V-ATPase function is regulated *in vivo* by a unique mechanism referred to as reversible disassembly, a condition under which the enzyme dissociates into membrane-bound V_o and cytoplasmic V_1 sectors (26, 27) (Fig. 1). Reversible dissociation of V-ATPase is well characterized in the model organism *S. cerevisiae* (28), but more recent data suggest that the mammalian enzyme is regulated by a similar process in some cell types (5, 29–31). Although the assembly status of yeast V-ATPase is mainly governed by nutrient availability (32), the situation in mammalian cells appears to be more complex. Besides glucose levels (30), V-ATPase assembly in animal cells can be induced by a variety of signals, including cell maturation (33) and stimulation by hormones (34) and growth factors (6). Upon enzyme dissociation, the activity of both sectors is silenced; that is, the V_1 no longer hydrolyzes MgATP (35, 36), and the V_o no longer translocates protons (37, 38). Although studies in yeast suggest that V_1 activity silencing depends on the C-terminal domain of subunit H, possibly together with inhibitory MgADP (35, 39, 40), the mechanism by which passive proton transport across V_o is blocked is less well understood.

The structure of eukaryotic V-ATPase has been analyzed by EM, and together with crystal structures of individual subunits and subcomplexes from yeast V-ATPase and related bacterial enzymes, the EM reconstructions have allowed generation of pseudoatomic models of the intact enzyme (22, 41, 42) and its functional V_1 (43) and V_o (38, 44) sectors. Although the resulting structural models together with biochemical data provide valuable information on the mechanism of ATP hydrolysis-driven proton pumping, we only have a limited understanding of the mechanism of reversible enzyme dissociation and reassociation. We recently obtained a cryo-EM reconstruction of yeast V_o (38), and although a comparison with EM models of holo V-ATPase showed that a_{NT} undergoes a large structural change to bind the rotor subunit *d* in free V_o, the resolution of the model was insufficient to precisely define the a_{NT}-*d* interface.

Here we present a negative-stain 3D EM reconstruction of lipid nanodisc-reconstituted V_o calculated at a resolution of ~15 Å. The model of nanodisc-bound V_o suggests that the interaction between a_{NT} and subunit *d* is mediated by charge complementation between acidic and basic residues on *d* and a_{NT}, respectively. Site-directed mutagenesis and isothermal titration calorimetry experiments conducted with recombinant subunits identified acidic and basic patches on *d* and a_{NT} that mediate the a_{NT}-*d* interaction. A comparison with the recent EM reconstructions of yeast V-ATPase in three states (22) suggests that, upon enzyme dissociation, free V_o is halted in state 3. We showed previously that autoinhibited, membrane-detached V_1-ATPase is halted in state 2 (45), and we propose that this conformational mismatch to state 3 V_o could function to prevent unintended reassembly of holo V-ATPase under conditions when the proton pumping activity of the enzyme is not needed.

Results

Purification of V_o Membrane Sector and Reconstitution into Lipid Nanodiscs—We previously developed a procedure for purification of milligram amounts of yeast V-ATPase V_o sector for functional and structural studies (38). Briefly, V_o was solubilized from vacuolar membranes and affinity-captured via a calmodulin binding peptide fused to the C terminus of the vac-

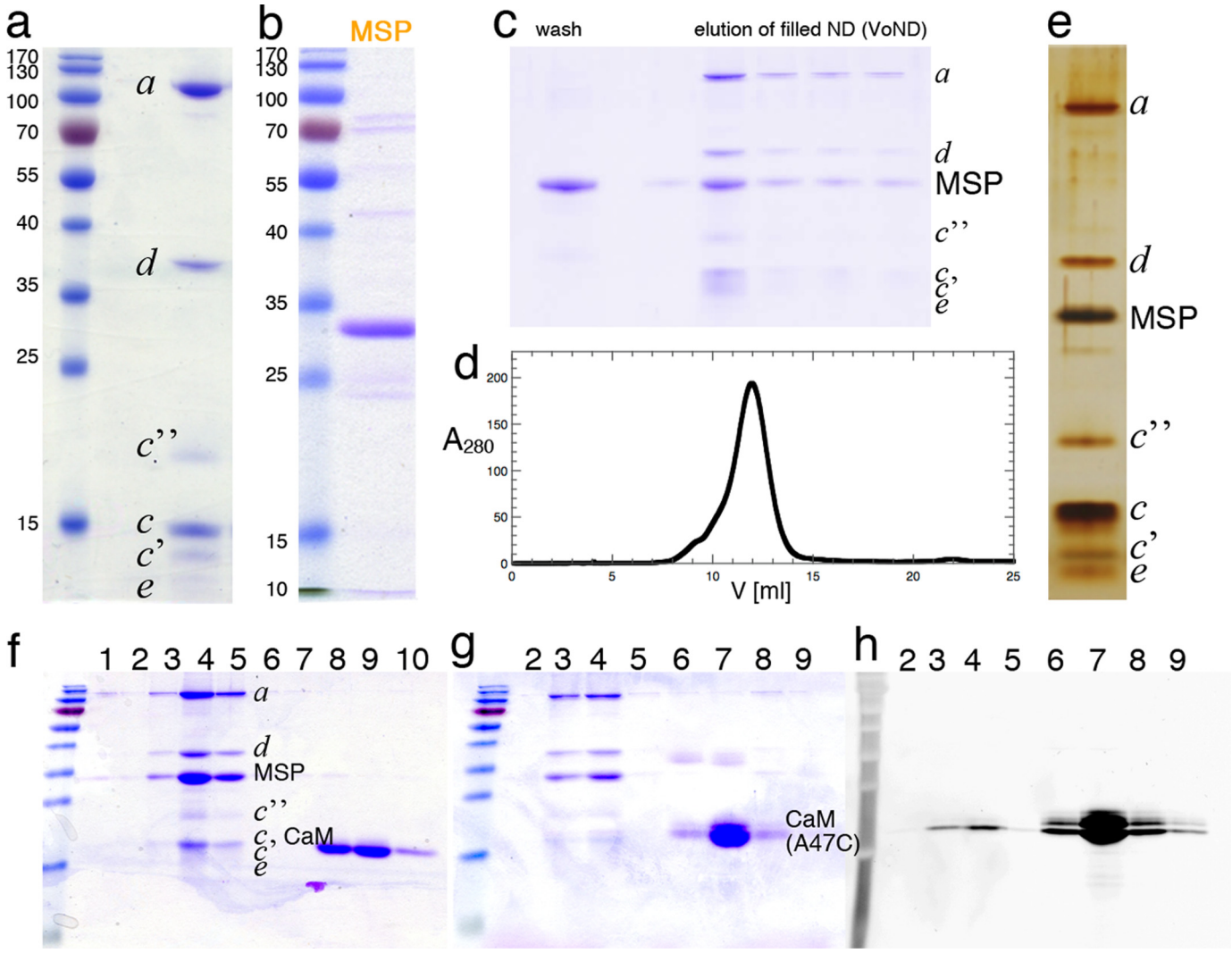

FIGURE 2. **Purification of V_o and reconstitution into lipid nanodiscs.** *a*, SDS-PAGE of yeast V_o affinity-purified from solubilized yeast microsomal membranes via a calmodulin binding peptide fused to the C terminus of subunit *a*. *b*, SDS-PAGE of the membrane scaffold protein MSP1E3D1, purified by affinity chromatography via an N-terminal His_6 tag. *c*, SDS-PAGE of flow-through and elution fractions from the calmodulin column after nanodisc reconstitution to remove unfilled discs. Reconstitution of the V_o into lipid nanodiscs is accomplished by mixing V_o, MSP, and lipid. Upon removal of detergent, V_o self-assembles into a nanodisc bilayer patch. *d*, size exclusion chromatography of V_oND after removal of unfilled discs. *e*, SDS-PAGE of the final preparation after gel filtration. *f*, glycerol gradient of V_oND-CaM. V_oND was mixed with a 5-fold excess of calmodulin, and the mixture was applied to a discontinuous 15–35% glycerol gradient and centrifuged at 200,000 × *g* for 16 h at 4 °C. Fractions were collected from the bottom of the gradient and analyzed by SDS-PAGE. Peak fractions (4, 5) were pooled and used for negative stain electron microscopy. *g* and *h*, to verify binding of calmodulin to V_oND, calmodulin (*A47C*) was labeled with fluorescein maleimide and the mixture of V_oND, and labeled calmodulin was subjected to glycerol density centrifugation as in *f*. *h*, the fluorescence scan of the gel shown in *g* indicates co-migration of labeled calmodulin with V_oND. The gels in *a*–*c*, *f*, and *g* were stained with Coomassie blue; the gel in *e* was stained with silver.

uole-specific isoform of subunit *a* (Vph1p). For structural studies under more native-like conditions, V_o was reconstituted into lipid nanodiscs as described under "Experimental Procedures" (Fig. 2). Purified detergent-solubilized V_o (Fig. 2*a*) was mixed with *Escherichia coli* polar lipids and the recombinant membrane scaffold protein MSP1E3D1 (Fig. 2*b*), followed by detergent removal with polystyrene beads. In a final purification step, V_o-containing nanodiscs (V_oND) were separated from "empty" discs by a second calmodulin affinity binding step followed by size exclusion chromatography on a Superdex S200 column (Fig. 2, *c* and *d*). Peak fractions of V_oND eluted from the gel filtration column were pooled, and the concentrated preparation was analyzed by SDS-PAGE and silver staining (Fig. 2*e*).

3D EM Reconstruction of V_oND—We initially generated a dataset of ~30,000 particles from EM images of negatively stained V_oND. However, attempts to reconstruct a 3D model of the complex using reference-free algorithms were unsuccessful, likely because of the limited size of the complex and the lack of characteristic features required for alignment. Models did not converge on a specific handedness, *i.e.* orientation of a_{NT} with respect to the membrane sector, and density for a_{NT} was smeared out over the membrane and did not allow us to distinguish its positioning relative to subunit *d*. We therefore decided to make use of the calmodulin binding peptide on the C terminus of subunit *a* to introduce an additional asymmetry to aid in alignments and angle determination in the 3D startup procedure. Purified calmodulin (CaM) was incubated with V_oND, followed by removal of excess CaM using glycerol gradient centrifugation (Fig. 2, *f*–*h*). Negative stain electron microscopy showed that the final V_oND-CaM preparation was monodis-

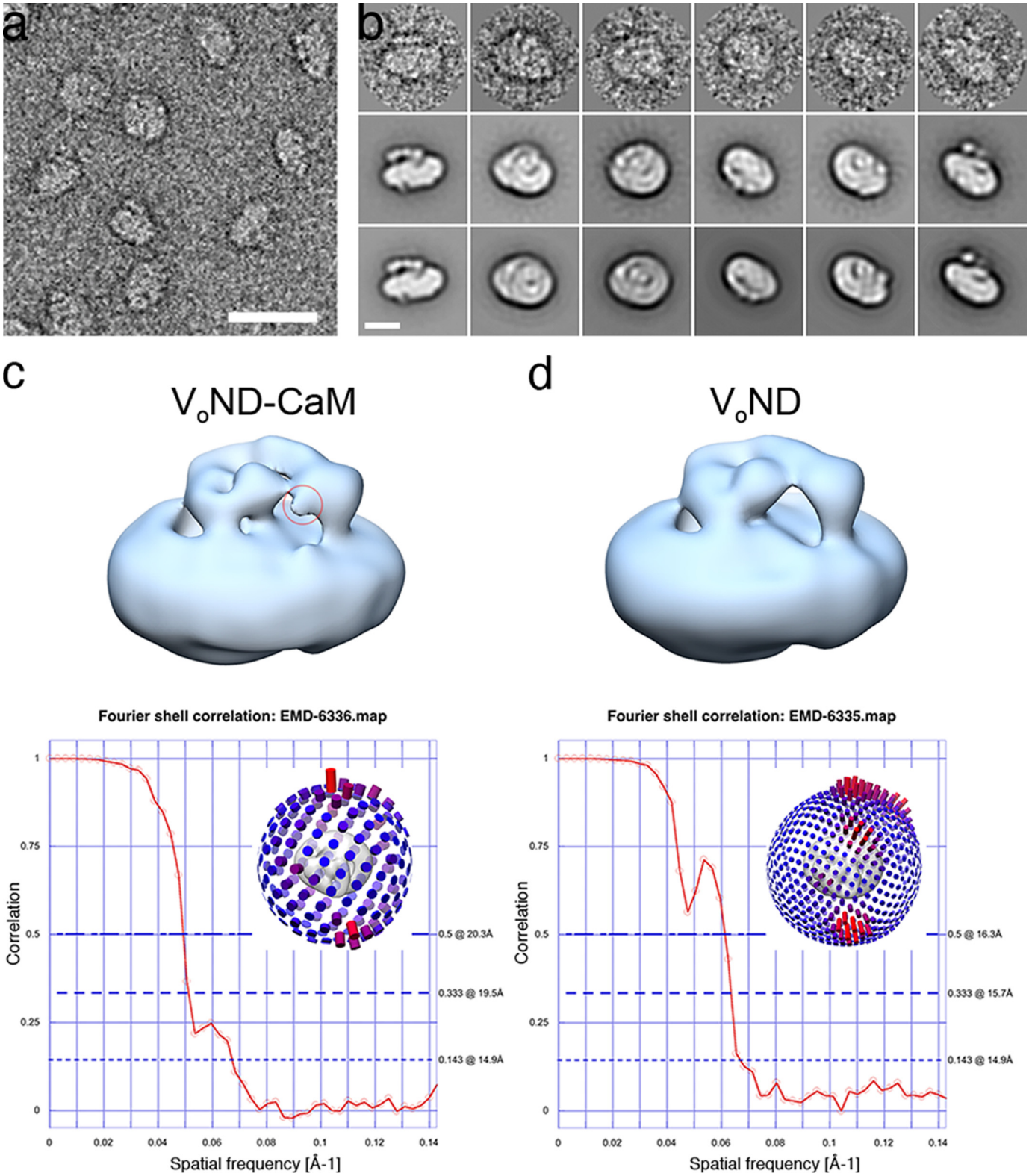

FIGURE 3. **Negative stain transmission electron microscopy of V_oND-CaM.** *a*, the representative micrograph reveals a monodisperse sample of ~12-nm particles. *b*, class averages obtained by reference-free alignment of a dataset of ~40,000 V_oND-CaM projections (*center row*) with corresponding raw particle images (*top row*) and reprojections of the final V_oND-CaM reconstruction (*bottom row*). *c* and *d*, final 3D reconstructions of V_oND-CaM (*c*) and V_oND (*d*) with corresponding gold standard FSC graphs shown below the models. The *red circle* on the V_oND-CaM reconstruction indicates the density for calmodulin bound to the C terminus of subunit *a*. *Insets* in the FSC graphs illustrate the angular distributions of the particle orientations of the two datasets. Scale bars = 20 nm (*a*) and 10 nm (*b*).

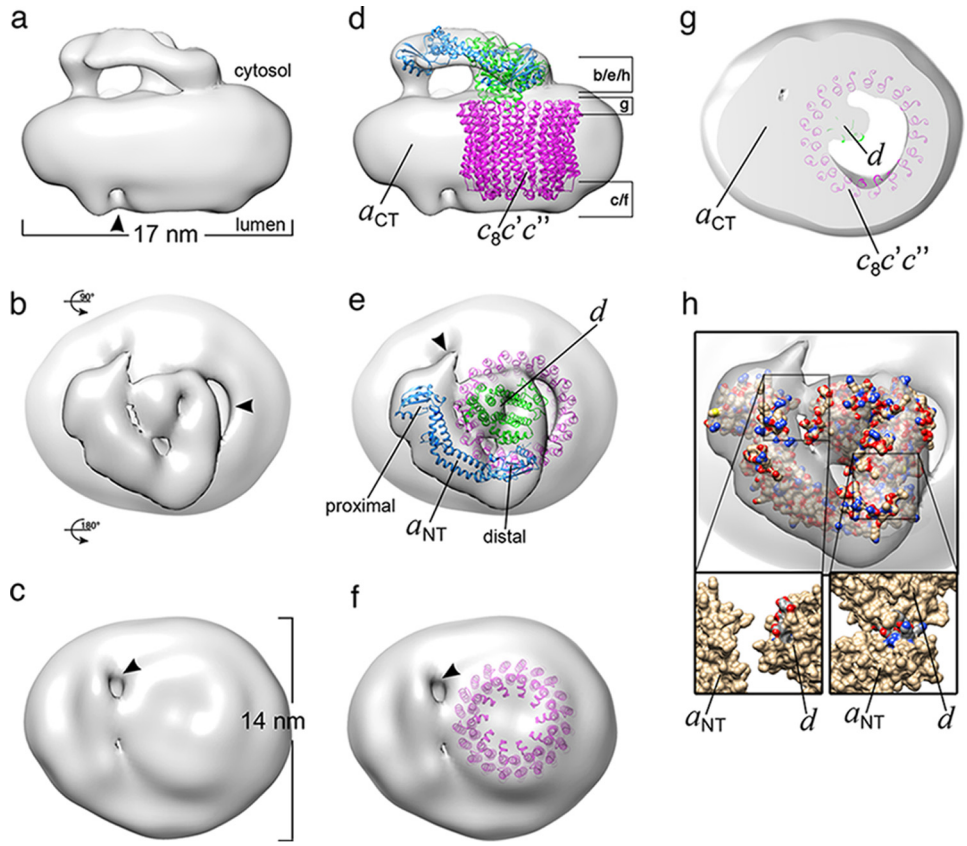

FIGURE 4. **3D reconstruction of V_oND-CaM.** *a–c*, side (*a*), top (*b*), and bottom (*b*) views of the 3D model of V_oND-CaM. The membrane sector is ~17 × 14 nm (*a* and *c*) with density on the cytosolic side above the membrane (a_{NT} and subunit *d*) and a cleft on the lumenal side (*arrowhead* in *a*). *d–f*, fit of homology models of V_o subunits into the EM density: a_{NT} (threaded into the crystal structure of *M. ruber* I_{NT}, PDB code 3RRK) in *cyan*, subunit *d* (threaded into the crystal structure of *T. thermophilus* C, PDB code 1V9M) in *green*, and *E. hirae* K_{10} (PDB code 2BL2) in *magenta*. *g*, cross-section as indicated in *d*, showing that the density representing the N-terminal α helix of subunit *d* contacts only one side of the *c*-ring as seen in state 3 of holo V_1V_o (22). *h*, top view of V_oND-CaM fitted with atomic models to indicate the sites of contact between a_{NT} and subunit *d*. Note that, because of its pseudo-3-fold symmetry, the homology model of subunit *d* could be placed into the EM density in three orientations corresponding to the orientations as described for states 1–3 (22), with orientations 2 and 3 resulting in much better model-map correlations compared with orientation 1. The model (Phyre model of yeast "*d*") to map (V_oND-CaM; EMD-6336) correlations for the three orientations were 0.081 for state 3, 0.085 for state 2, and 0.076 for state 1, with 404, 296, and 323 amino acids outside of the model at a contour level of 0.022 for states 1–3, respectively.

perse, with an average diameter of the particles of ~12 nm (Fig. 3*a*). A dataset of ~40,000 particles, generated from 380 micrographs such as shown in Fig. 3*a*, was subjected to reference-free alignment procedures as implemented in EMAN2. Fig. 3*b* shows class averages of side, top, and intermediate view projections (*center row*), representative raw particle images (*top row*), and the corresponding reprojections of the final 3D model (*bottom row*). Class averages, including those shown in Fig. 3*b*, were used for a 3D startup procedure in EMAN2, and the resulting 3D reconstruction was refined until stable. At this point, the reconstruction was strongly low pass-filtered and used as input for the 3D autorefinement procedure as implemented in the Relion 1.3 software package. The model was then refined until no further improvement was observed. The resolution of the final V_oND-CaM 3D reconstruction was estimated to be 14.9 Å (20.3 Å at 0.5 correlation) using the "gold standard" FSC protocol as implemented in Relion 1.3 (Fig. 3*c*).

The final V_oND-CaM model was strongly low pass-filtered to serve as a reference for a new V_oND dataset (~47,000 images) using the Relion 3D autorefinement procedure as described for the V_oND-CaM dataset. The 3D autorefinement converged to a final model of V_oND with an estimated gold standard resolution of ~14.9 Å (16.3 Å at 0.5 correlation, Fig. 3*d*). As can be seen from Fig. 3, *c* and *d*, the final V_oND-CaM and V_oND models are very similar except for a small density in the V_oND-CaM map that is due to the CaM bound at the *a* subunit C terminus (Fig. 3*c*, *top panel*, *red circle*). However, because the V_oND-CaM map showed slightly more detail, we used this model to illustrate the features of nanodisc-bound V_o as summarized in Fig. 4.

Side, top, and bottom views of the V_oND-CaM model are illustrated in Fig. 4, *a–c*, showing the characteristic features as seen in earlier reconstructions of bovine (44) and yeast (38) V_o, including the densities above the membrane (a_{NT} and subunit *d*), the cleft between the density for a_{CT} and the *c*-ring (Fig. 4*a*, *arrowhead*), which opens into a solvent (stain)-accessible pore as seen in the bottom view (Fig. 4*c*, *arrowhead*), and the large cavity on the cytoplasmic side of the *c*-ring (Fig. 4*b*, *arrowhead*). Semiautomatic fitting of homology models of the yeast V_o subunits into the EM density is summarized in Fig. 4, *d–f*. As illustrated in Fig. 4, *d* and *e*, a_{NT} (*blue*) was positioned with its proximal lobe (which is comprised by the N and C termini of subunit *a*, domain nomenclature as in Ref. 46) near the connection point to the membrane-bound a_{CT}, placing its distal lobe near the central density corresponding to subunit *d* (*green*).

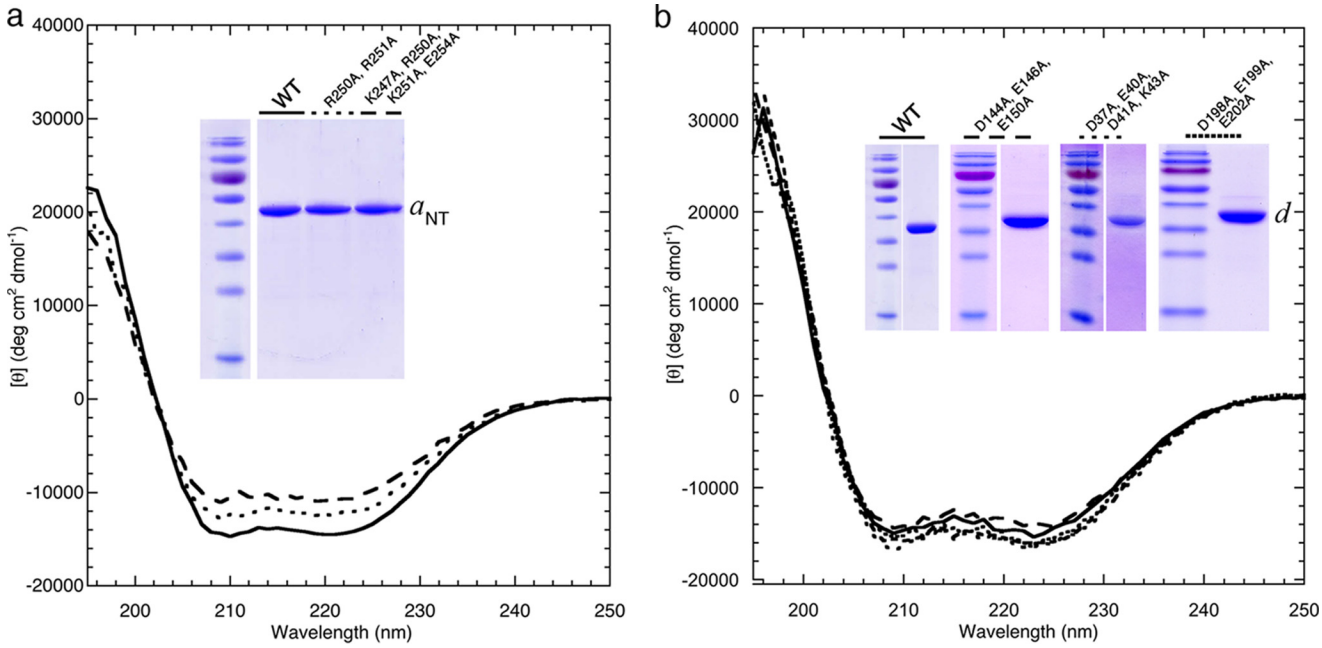

FIGURE 5. **Purification and circular dichroism spectroscopy of recombinant wild-type and mutant $a_{NT(1–372)}$ and subunit *d*.** *a*, Coomassie-stained SDS-PAGE and CD spectroscopy of the wild type and mutant $a_{NT(1–372)}$ constructs expressed and purified as described under "Experimental Procedures." *b*, SDS-PAGE and CD spectra of the wild type and mutant subunit *d*. The two minima at ~208 and 222 nm in the CD spectra of both the wild type and mutant $a_{NT(1–372)}$ and subunit *d* constructs indicate α-helical secondary structure. CD wavelength scans were collected from 250–195 nm in 25 mM sodium phosphate (pH 7) at 10 °C (0.1 mM TCEP was included in the buffer for the subunit *d* scans). SDS-PAGE gels were loaded with ~3 μg of the wild type or mutant subunits.

Because of its pseudo-3-fold symmetry and the limited resolution of the EM reconstruction, the yeast subunit *d* homology model could be fit in three orientations corresponding to rotational states 1, 2, and 3, as seen in the recent cryo-EM reconstructions of intact yeast V-ATPase (22). However, only the orientation corresponding to state 3 preserved the contact between the subunit *d* N-terminal α helix and the cytoplasmic face of the *c* subunit ring, as seen in the recent cryo-EM model of holo V-ATPase in state 3 (22) (Fig. 4*g*), and we therefore explored the contacts between a_{NT} and *d* predicted by this configuration (Fig. 4*h*, see below). For filling the density corresponding to the yeast *c*-ring, we used the crystal structure of the K_{10} ring from *Enterococcus hirae* (47) (Fig. 4*h*, *magenta*).

Interaction of a_{NT} and Subunit d—We previously reported a 3D reconstruction from cryo-EM images of detergent-solubilized yeast V_o that showed a_{NT} and subunit *d* in close proximity (38). Although subsequent binding studies using recombinant a_{NT} (residues 1–372, $a_{NT(1–372)}$) and *d* revealed a K_d of the $a_{NT(1–372)}$-*d* interaction of ~5 μM (38), the resolution of the cryo-EM model, was insufficient to define the binding site(s) between a_{NT} and *d* in detail. Fig. 4*h* illustrates the interface between a_{NT} and subunit *d* based on the fitting of the homology models into the EM density of the V_oND-CaM model presented here. As can be seen, a_{NT} and subunit *d* appear to contact each other via two distinct sites near the proximal and distal lobes of a_{NT} (Fig. 4*h*). The contact near the distal lobe (Fig. 4*h*, *bottom right*) is mediated by two short α helices, one from a_{NT} (residues 242–256, yeast subunit *a* isoform Vph1p) and one from subunit *d* (residues 144–154). The other site near the proximal lobe of a_{NT} is mediated by a short helix-turn-helix motif in *d* (residues 38–58) and a less well defined face in a_{NT} (Fig. 4*h*, *bottom left*). Many of the acidic and basic residues involved in these two contact sites are highly conserved from yeast to human (see isothermal titration calorimetry sections below). Considering the conserved nature of the charged residues, we reasoned that complex formation between a_{NT} and *d* could be driven by electrostatic interactions involving the conserved residues. To test this hypothesis, we generated a_{NT} double (R250A,K251A) and quadruple mutants (K247A,R250A, K251A,E254A) in the short α helix in the distal lobe of a_{NT} and triple (D144A,E146A,E150A) and quadruple (D37A,D40A,D41A, K43A) mutants in subunit *d* for *in vitro* binding experiments using isothermal titration calorimetry (ITC). As a negative control, we generated a triple mutant of *d* in an area predicted to be outside of the a_{NT}-*d* contact area (E198A,E199A,E202A).

The wild type and alanine mutants of $a_{NT(1–372)}$ and subunit *d* were expressed as N-terminal fusions with maltose binding protein (MBP) connected via a protease cleavage site as described previously (38). The proteins were purified away from MBP via anion exchange and size exclusion chromatography. Purity and proper folding of the resulting $a_{NT(1–372)}$ and subunit *d* constructs was confirmed by Coomassie-stained SDS-PAGE and CD spectroscopy, respectively (Fig. 5, *a* and *b*). As can be seen from the CD spectra, all $a_{NT(1–372)}$ and subunit *d* mutant proteins showed minima at 208 and 222 nm similar to the wild-type subunits and characteristic for highly α-helical proteins, indicating that the mutations did not interfere with proper folding of the recombinant subunits.

Isothermal Titration Calorimetry of Mutant $a_{NT(1–372)}$ and Wild-type d—We first conducted ITC titrations with double and quadruple mutants of the conserved charged residues in

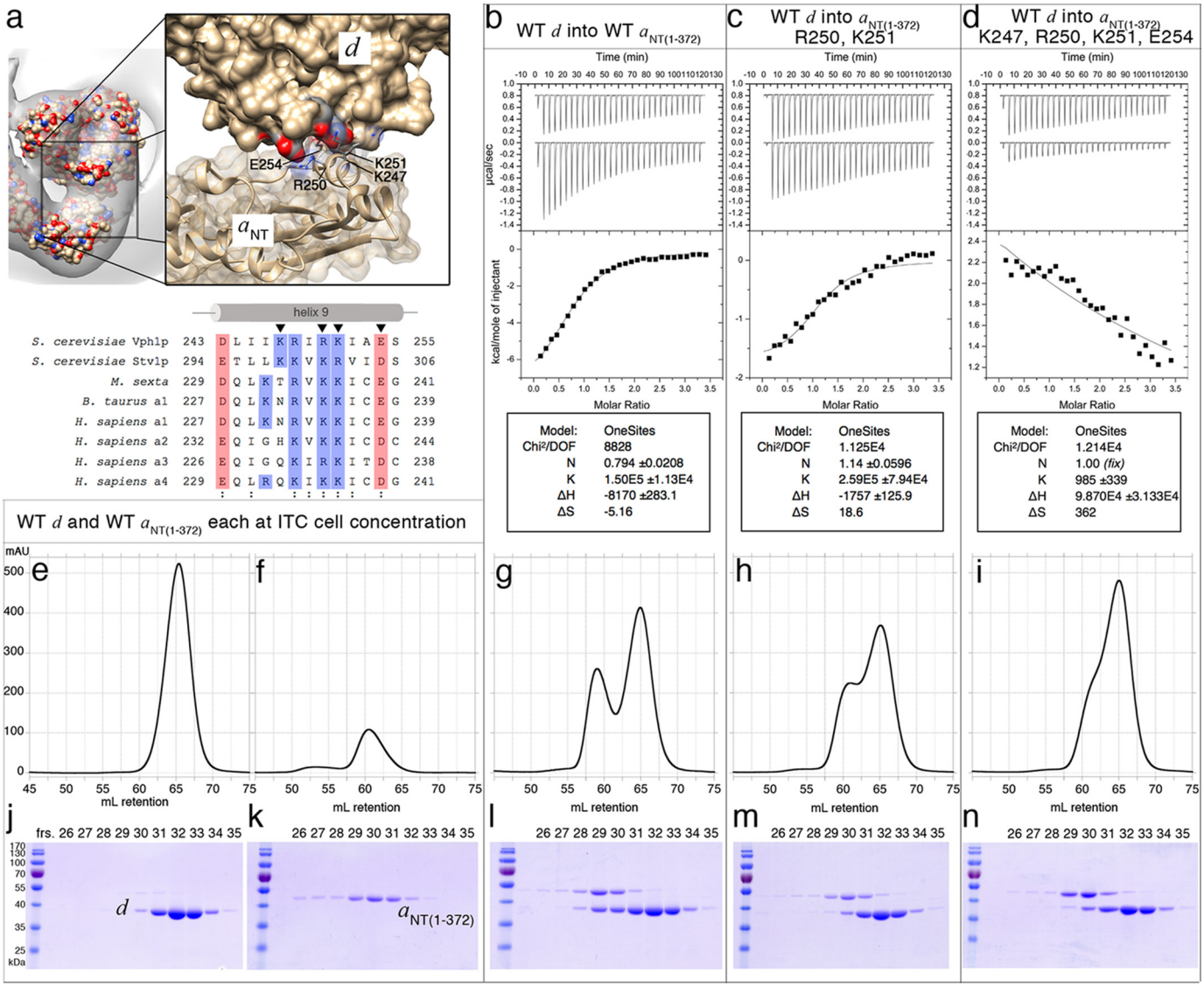

FIGURE 6. **Isothermal titration calorimetry of the interaction between subunit *d* and wild-type and mutant $a_{NT(1-372)}$.** *a*, *top panel*, detailed view of the a_{NT}/*d* contact as shown in Fig. 4*h*, *bottom right*, indicating that the distal lobe of a_{NT} appears to be participating in an interaction with subunit *d* via a short charged α helix in a_{NT} to a largely acidic face of subunit *d*. *a*, *bottom panel*, the four residues of the short α helix facing subunit *d* are Lys-247, Arg-250, Lys-251, and Glu-254, which belong to a patch of charged residues mostly conserved through higher eukaryotes, as shown by the sequence alignment of helix 9 of subunit *a*. *b–d*, isothermal titration calorimetry of subunit *d* and $a_{NT(1-372)}$ constructs (representative titrations of two repeats). Titration of subunit *d* into wild-type $a_{NT(1-372)}$ (*b*), $a_{NT(1-372)}$ (R250A,K251A) (*c*), and $a_{NT(1-372)}$ (K247A,R250A,K251A,E254A) (*d*). *e–i*, subunit *d* and $a_{NT(1-372)}$ alone as well as the cell contents of the completed titrations were subjected to size exclusion chromatography on Superdex 200 (16 × 500 mm) with the corresponding SDS-PAGE gels shown in *j–n*. For details, see text.

the short α helix of the a_{NT} distal domain that were facing subunit *d* (Fig. 6*a*). Titrating subunit *d* into wild-type $a_{NT(1-372)}$ revealed an exothermic binding reaction (Fig. 6*b*). Fitting the data with a single-site binding model revealed a ~1:1 stoichiometry with a K_d of 6.7 μM, similar to what we obtained earlier by titrating $a_{NT(1-372)}$ into subunit *d* (38). The ΔH and ΔS were −34.2 kJ/mol and −21.6 J·(mol·K)$^{-1}$, respectively, giving a ΔG of the enthalpy-driven binding reaction of −28.1 kJ/mol. Titrating subunit *d* into the double $a_{NT(1-372)}$ mutant (R250A,K251A) produced significantly less heat (ΔH = −7.4 kJ/mol), but, at the same time, the K_d was similar compared with the wild-type proteins (K_d = 4 μM, Fig. 6*c*) and appeared to be partly driven by entropy (ΔS = 77.8 J·(mol·K)$^{-1}$, ΔG = −29.4 kJ/mol). On the other hand, titrating subunit *d* into the quadruple mutant of $a_{NT(1-372)}$ (K247A,R250A,K251A,E254A) resulted in a weak endothermic reaction that could not be fit to a single site model without fixing the stoichiometry at 1:1 (Fig. 6*d*). Under these conditions, the K_d was ~1 mM, indicating that replacement of all four conserved charged residues by alanines disrupted the interaction between $a_{NT(1-372)}$ and *d*.

The cell contents of the ITC experiments (with titrated wild-type $a_{NT(1-372)}$, double mutant, and quadruple mutant) were subjected to size exclusion chromatography as described under "Experimental Procedures." Subunit *d* and $a_{NT(1-372)}$ alone eluted at 65 and 60 ml, respectively (Fig. 6, *e* and *f*). Note that although subunit *d* alone runs as a monodisperse monomer (Fig. 6, *e* and *j*), $a_{NT(1-372)}$ exists in a concentration-dependent monomer-dimer equilibrium as reported earlier (38) and as evident from its elution profile and accompanying SDS-PAGE gel

(Fig. 6, *f* and *k*). The elution profile of the mixture of wild-type $a_{NT(1–372)}$ and *d* revealed two peaks at 58 and 65 ml (Fig. 6*g*), and analysis by SDS-PAGE showed that the peak around 58 ml (fraction 29) contained close to stoichiometric amounts of $a_{NT(1–372)}$ and *d* (Fig. 6*l*). The relatively small shift of 2 ml (one fraction) toward larger molecular size is consistent with the moderate K_d of the $a_{NT(1–372)}$-*d* complex formation of 6.7 μM and in close agreement with our previous study (38).

In the size exclusion profile of the double mutant titration (subunit *d* into $a_{NT(1–372)}$ R250A,K251A), the interacting peak is shifted slightly to a larger volume at ~61 ml as a shoulder of the subunit *d* peak (~66 ml) (Fig. 6*h*), indicating a weakening of the $a_{NT(1–372)}$-*d* interaction and consistent with the reduced binding enthalpy and the SDS-PAGE gel of the peak fractions (Fig. 6*m*). This trend is continued for the titration of the quadruple mutant (subunit *d* into $a_{NT(1–372)}$ K247A,R250A,K251A, E254A), which only shows a shoulder for a_{NT} unresolved from the subunit *d* peak (Fig. 6*i*) with elution profiles similar to the individual subunits (Fig. 6*n*). Taken together, the ITC and gel filtration data showed that mutation of the conserved charged residues on the short α helix in the distal domain of a_{NT} disrupts the a_{NT}-*d* interaction.

Isothermal Titration Calorimetry of Mutant d and Wild-type $a_{NT(1–372)}$—As mentioned above, subunit *d* appears to contact a_{NT} at two sites, the short α helix in the distal domain and at a second site near the proximal domain (Fig. 4*h*). To verify the fit of subunit *d* in the EM model and to test whether the contact site near the proximal lobe of a_{NT} contributes to the interaction between the two subunits, we generated triple and quadruple mutants of subunit *d* by replacing conserved charged residues that are facing a_{NT} from the two sites on *d* (Fig. 7, *a* and *e*). ITC titrations of both triple (Fig. 7*b*) and quadruple (Fig. 7*f*) alanine mutants of *d* with wild-type $a_{NT(1–372)}$ revealed weak endothermic reactions that could not be fit to a single site binding model without fixing $n = 1$. Under these conditions, the K_ds for the two titrations of the triple and quadruple mutants of *d* were ~0.25 mM and ~1.7 mM, respectively. Consistent with the ITC titrations, gel filtration profiles (Fig. 7, *c* and *g*) and SDS-PAGE of the peak fractions (Fig. 7, *d* and *h*) indicated elution of non-interacting subunits. Contrary to the alanine mutations of residues predicted to be in the a_{NT}-*d* binding interface (Fig. 7, *a–h*), mutagenesis of a patch of acidic residues outside the interface (E198A,E199A,E202A) did not interfere with complex formation (Fig. 7, *i–l*). Taken together, the ITC and gel filtration experiments showed that both contact sites between a_{NT} and *d* as seen in the EM fit contribute to the binding interaction between the two subunits. However, because disrupting either of the two sites weakened the interaction beyond detection by ITC or gel filtration, this suggests that the individual interactions are weak and that only the combined *avidity* of the two interactions results in a measurable *affinity*.

Discussion

We have developed a protocol to reconstitute purified V-ATPase V_o membrane sector into lipid nanodiscs. When reconstituted into nanodiscs, V_o is stable, as evident from the lack of subunit *a* degradation products (Fig. 2*e*) sometimes seen in the detergent-solubilized complex (38). Negative stain EM showed that the preparation is monodisperse, and we were able to reconstruct 3D models of the nanodisc-bound V_o with and without calmodulin bound to the calmodulin binding peptide at the C terminus of subunit *a*. Fitting of a_{NT} and subunit *d* homology models into the EM density revealed that the two subunits are in contact, as described previously for the negative stain and cryo-EM models of detergent solubilized bovine and yeast V_o, respectively (38, 44). However, the slightly better resolution of the V_oND models allowed us to identify two sites of contact between a_{NT} and *d*, both involving charged and highly conserved residues. ITC analysis of triple and quadruple alanine mutants of a_{NT} and *d* confirmed the involvement of the charged residues in the interaction, but the analysis also showed that the individual interactions are weak and that only the combined avidity of both binding sites leads to a measurable K_d of ~6 μM (Ref. 38 and the data presented here). As mentioned under "Introduction," V-ATPase is regulated by a reversible disassembly mechanism that results in membrane-detached V_1 and membrane-bound free V_o. A relatively moderate affinity between *d* and a_{NT} can be rationalized by the fact that this interaction has to be broken when reassembly of holo V-ATPase is initiated.

A comparison of the V_oND 3D models with the recent cryo-EM reconstructions of holo V-ATPase in three states (22) revealed that free V_o appears to be halted in rotary state 3 based on the orientation of subunit *d* relative to a_{NT}. As mentioned under "Results," because of the limited resolution of the V_oND 3D models and because of the pseudo-3-fold symmetry of subunit *d*, *d* could also be fit in the state 2 orientation with a comparable model-map correlation compared with the state 3 fit (the fit of state 1 is of much lower quality, see Fig. 4). The ITC data, however, are only consistent with the state 3 orientation. Furthermore, only the state 3 orientation preserves the contact between the N-terminal α helix of *d* and the cytoplasmic loops of the proteolipid ring, as seen in the models of all three states of the holo enzyme (22). Taken together, the data therefore indicate that free V_o is halted in a single conformation corresponding to state 3 of holo V-ATPase.

Recently, we determined the 6.2- to 6.5-Å crystal structure of autoinhibited yeast V_1-ATPase (40). Interestingly, a comparison of the structure of autoinhibited V_1 with the structure of V_1 as part of holo V-ATPase (22) revealed that the membrane-detached V_1 is halted in state 2 based on the rotational position of the DF rotor relative to the inhibitory H subunit (40). The observation that autoinhibited V_1 is halted in state 2 together with the findings presented here that free V_o is halted in state 3 indicates that there is a conformational mismatch between the two complexes as a result of regulated enzyme disassembly. We speculate that this mismatch may serve to prevent unintended reassembly of the enzyme when the disassembled state is required. How this mismatch is relieved when reassembly is required is not known, but it is possible that V_1 binding to the assembly chaperone regulator of the H^+-ATPase of vacuolar and endosomal membranes (RAVE) (48) changes V_1 conformation to enable V_o binding. Another possibility is that the V_o conformation is altered by interac-

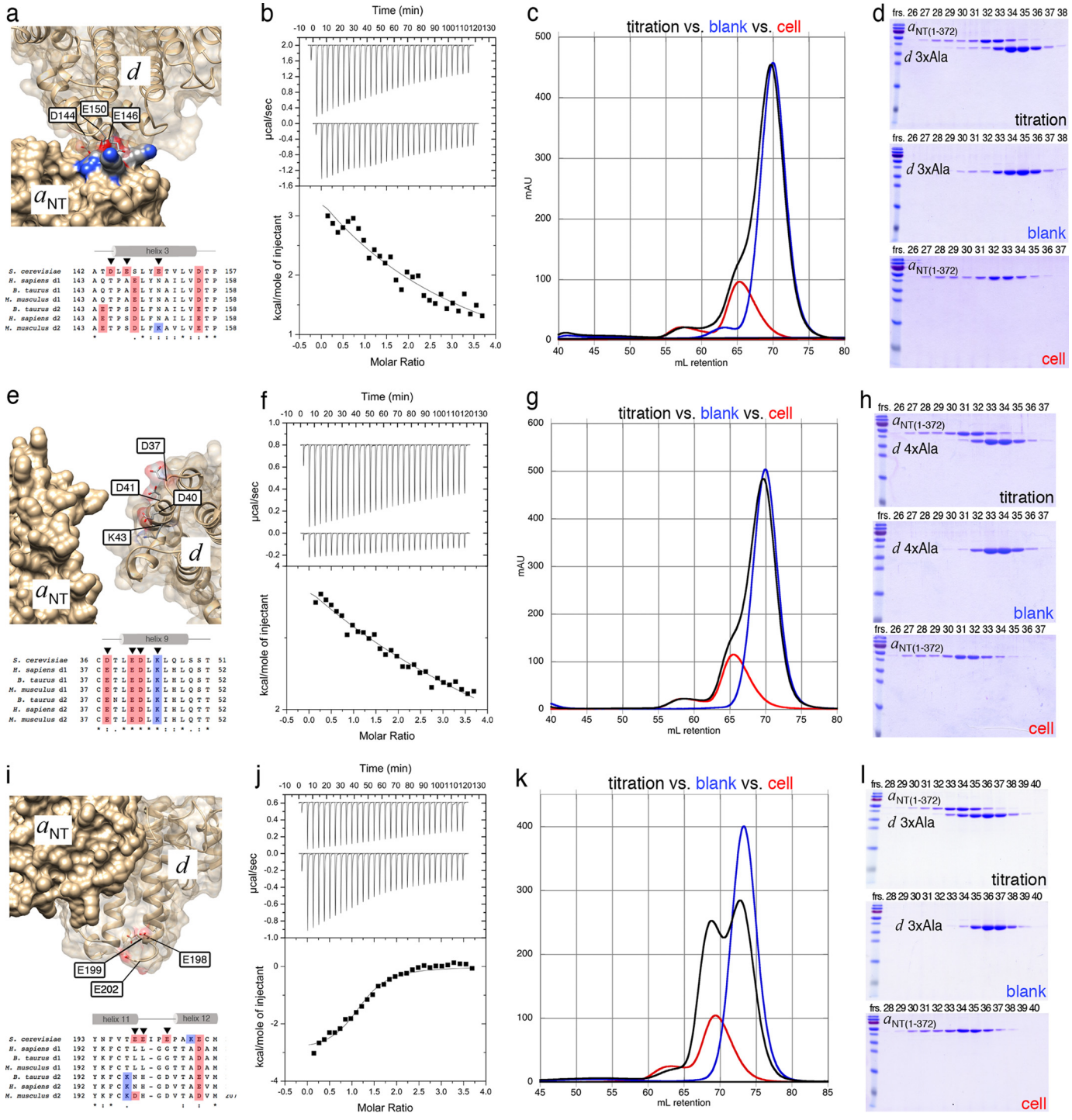

FIGURE 7. **Isothermal titration calorimetry of the interaction between wild-type $a_{NT(1-372)}$ and mutant subunit *d*.** *a* and *e*, close-up of the contact between *d* and the a_{NT} distal (*a*) and proximal (*e*) lobe. *b–d*, ITC (*b*), gel filtration (*c*), and SDS-PAGE (*d*) of the *d* triple mutant (D144A,E146A,E150A) with $a_{NT(1-372)}$. *f–h*, ITC (*f*), gel filtration (*g*), and SDS-PAGE (*h*) of the *d* quadruple mutant (D37A,E40A,D41A,K43A) with $a_{NT(1-372)}$. *i–l*, as a negative control, a subunit *d* mutant with acidic residues (Glu-198, Glu-199, and Glu-202) outside of the predicted interface with a_{NT} changed to alanines was titrated with wild-type $a_{NT(1-372)}$. Fitting the data revealed a K_a of $\sim 4 \times 10^5 \pm 8 \times 10^4$ M ($K_d \sim 2.5$ μM; N $\sim$ 1.2; $\Delta H = -12.4 \pm 0.49$ kJ/mol; $\Delta S \sim 63$ J·(mol·K)$^{-1}$). Shown are representative ITC titrations of at least two repeats for each mutant. Note that the gel filtration column was repacked after the experiments in Fig. 6, resulting in a slightly different elution volume for the recombinant subunits for the two sets of titrations shown in Figs. 6 and 7.

tion with specific phosphoinositides that have been shown to bind to V_o and promote enzyme assembly on the vacuolar membrane (49).

Here we have shown that yeast V_o can be reconstituted into lipid nanodiscs, resulting in a highly monodisperse preparation that is amenable to structure determination by single-molecule EM. Future studies using cryo-EM will allow high-resolution structural studies of the complex in a more native environment compared with the detergent-solubilized state, allowing, for example, an examination of the interaction with specific lipid molecules that have been shown to be either essential for V-ATPase function (50) or

involved in the mechanism of reversible enzyme disassembly (49). These studies are ongoing in our laboratory.

Experimental Procedures

Reagents—Undecyl-β-D-maltoside (UnDM) was from Anatrace. *E. coli* polar lipid extract was obtained from Avanti. Calmodulin-Sepharose beads were from GE Healthcare or Agilent. CDTA was from Fisher Scientific. All other reagents were of analytical grade.

Purification of Yeast V_o—Cell growth of a yeast strain expressing subunit *a* isoform Vph1p with a C-terminal fusion of calmodulin binding peptide, membrane preparation, and V_o extraction and purification were performed as described previously (38) with the following modifications. Yeast cells were harvested during the second log phase by centrifugation at 2600 × *g*, washed in water, and resuspended in lysis buffer (25 mM Tris-HCl (pH 7.4), 500 mM sorbitol, and 2 mM EGTA), and broken in a Bead Beater (Omni International) using zirconium beads (BioSpec). After removing cell debris and mitochondria by low-speed (2500 × *g*, 10 min) and medium-speed (12,000 × *g*, 20 min) centrifugation, membranes were collected by ultracentrifugation (370,000 × *g*, 2 h), washed once in buffer (25 mM Tris-HCl (pH 7.4) and 500 mM sorbitol), and pelleted again (370,000 × *g*, 1 h). The total protein concentration of the membrane samples was determined by BCA protein assay (Thermo Scientific) of trichloroacetic acid-precipitated membranes. Isolated membranes were diluted to 10 mg/ml and stored at −80 °C until use.

Membranes were solubilized by addition of UnDM from a 20% stock solution in water to a final concentration of 0.6 mg of detergent/mg of membrane protein for 1 h with gentle agitation. Extracted membranes were supplemented with 4 mM $CaCl_2$ and centrifuged at 180,000 × *g* for 1 h to remove the insoluble fraction. The supernatant was then applied to a 5-ml calmodulin-Sepharose column pre-equilibrated in calmodulin washing buffer (10 mM Tris-HCl (pH 8), 150 mM NaCl, 2 mM $CaCl_2$, 10 mM β-mercaptoethanol, and 0.1% UnDM). The column was washed with 5 column volumes each of washing buffer and washing buffer without NaCl and eluted with elution buffer (10 mM Tris-HCl (pH 8), 10 mM CDTA, 10 mM β-mercaptoethanol, and 0.1% UnDM).

Preparation of Membrane Scaffold Protein—Membrane scaffold protein MSP1E3D1 (MSP) was expressed in *E. coli* BL21 (DE3) via a pET28a plasmid (Addgene, 20066) as described previously (51) with the following modifications. Briefly, the strain was grown to mid-log phase in terrific broth (25 g/liter Luria-Bertani-Miller broth (EMD Biosciences) supplemented with 0.4% (v/v) glycerol). Expression was induced with 1 mM isopropyl 1-thio-β-D-galactopyranoside (BioVectra) for 1 h at 37 °C, followed by 3.5 h at 28 °C. Cells were harvested by centrifugation, resuspended in lysis buffer (25 mM sodium phosphate (pH 8) and 1% Triton X-100) and lysed with a French press (Spectronic Unicam). Lysate was cleared by centrifugation (17,000 × *g*) and passed over a nickel-nitrilotriacetic acid affinity column (Qiagen). The column was washed in place with each of three buffers: 40 mM Tris-HCl, 300 mM NaCl, and 1% Triton X-100, pH 8); 40 mM Tris-HCl, 300 mM NaCl, 50 mM sodium cholate, and 5 mM imidazole (pH 8); and 40 mM Tris-HCl, 300 mM NaCl, and 10 mM imidazole (pH 8). Protein was eluted with a 10-column volume linear gradient of elution buffer (40 mM Tris-HCl, 300 mM NaCl, and 100 mM imidazole (pH 8)) and dialyzed against 40 mM Tris-HCl, 100 mM NaCl, and 0.5 mM EDTA (pH 7.4). MSP-containing fractions were pooled and concentrated by ultrafiltration using an Amicon cell with an XM50 filter membrane. Purified MSP was stored at −80 °C until use.

Lipid Nanodisc Reconstitution of V_o—E. coli total lipid extract (Avanti Polar Lipids) was suspended by sonication in disc-forming buffer (20 mM Tris-HCl (pH 7.4), 100 mM NaCl, and 0.5 mM EDTA) with the addition of 1 mM DTT (EMD Millipore). Detergent-solubilized V_o, purified MSP, and lipid were combined at a molar ratio of 0.02:1:25 with the addition of protease inhibitors, 1 mM PMSF, 1 mM leupeptin, 1 mM pepstatin, and 1 mM chymostatin (EMD Biosciences) and incubated at room temperature for 1 h with mixing. Prewashed Bio-Beads SM-2 (Bio-Rad) were added at 0.4 g/ml and incubated with mixing for 2 h at room temperature. The self-assembled nanodisc sample was recovered from the Bio-Bead mixture with a syringe. To remove unfilled (empty) nanodiscs (ND) from V_o-containing discs (V_oND), the reconstituted sample was supplemented with 10 mM $CaCl_2$ and applied to a 1-ml calmodulin resin column, washed with disc-forming buffer and eluted with the same buffer without $CaCl_2$ and supplemented with 10 mM CDTA. As a final polishing step, the eluted V_oND sample was concentrated to 2 ml, applied to a Superdex 200 HR 16/500 column on an AKTA FPLC (GE Healthcare) equilibrated with disc-forming buffer and eluted at 0.5 ml/min.

Preparation of Calmodulin—The gene for human calmodulin 1 was synthesized (BioBasic, Markham, ON, Canada) and cloned into a modified pMAL-c2E expression vector with a Prescission protease cleavage site between MBP and the N terminus of calmodulin. Briefly, *E. coli* Rosetta 2 harboring the calmodulin expression plasmid was grown to mid-log phase in rich broth (Luria broth supplemented with 0.2% glucose), and expression was induced with 1 mM isopropyl 1-thio-β-D-galactopyranoside for 18 h at 18 °C. Cells were harvested by centrifugation, resuspended in lysis buffer (20 mM Tris-HCl (pH 7.4), 200 mM NaCl, and 1 mM EDTA and lysed by sonication (Hielscher Ultrasonics). The lysate was cleared by centrifugation at 20,000 × *g* and passed over a pre-equilibrated amylose column (New England Biolabs). Bound protein was washed using the same buffer and eluted with the buffer supplemented with 10 mM maltose. Protein was cleaved using Prescission protease to remove the MBP tag and dialyzed into anion exchange buffer (20 mM Tris-HCl (pH 7.4), 1 mM EDTA, and 1 mM DTT). The sample was passed over a MonoQ anion exchange column attached to an FPLC and pre-equilibrated in buffer and eluted using a 30-column volume linear gradient of buffer to buffer plus 500 mM NaCl. Calmodulin-containing fractions were pooled, concentrated, and subjected to size exclusion chromatography (Superdex 75 16/500 column). For fluorescence detection of calmodulin, residue Ala-47 was changed to cysteine using QuikChange site-directed mutagenesis with the following primers: A47_fwd, GCC AGA ATC CAA CCG AAT GTG AAC TGC AAG ATA TGA TTA ACG; A47_rev, CGT TAA TCA TAT CTT GCA GTT CAC ATT CGG TTG GAT TCT GGC. For fluorescence detection, calmodulin (A47C) was

reacted with fluorescein maleimide for 1 h in the dark. Excess label was removed by a Sephadex G25 spin column.

Labeling of V_oND with Calmodulin—Purified calmodulin was added in a 5:1 molar ratio to V_oND, and the sample was loaded onto a discontinuous glycerol gradient (15–35% (v/v), 10 mM MOPS (pH 7), and 4 mM $CaCl_2$) for separation of unbound calmodulin. The gradient was subjected to centrifugation at 285,000 × *g* for 16 h. Afterward, 1-ml fractions were collected by fractionation from the bottom of the gradient and analyzed by SDS-PAGE.

Electron Microscopy—Carbon-coated copper grids were subjected to glow discharge in air for 45 s. Samples of V_oND and calmodulin-labeled V_oND (V_oND-CaM) at ~1 mg/ml were diluted 1:100 in 20 mM Tris-HCl (pH 7.4) and 150 mM NaCl supplemented with 0.5 mM EDTA or 4 mM $CaCl_2$, respectively, and applied to glow-discharged grids for 1 min, washed with water, and stained with 2% (w/v) uranyl formate (Electron Microscopy Science). Grids were observed in a JEOL JEM-2100 transmission electron microscope operating at 200 kV. Images were acquired on a charge-coupled device (F415MP, Tietz Video and Image Processing Systems GmbH) at a nominal magnification of ×60,000 and an underfocus of between ~1–2 μm. The calibrated pixel size on the specimen level was 1.75 Å.

Image Analysis and 3D Reconstruction—Single particles were selected (192 × 192 pixels) using e2boxer from EMAN2 with a semiautomated monitored picking procedure. Particles were phase flip-corrected for their contrast transfer functions by micrograph within the EMAN2 package. Datasets of 47,422 and 40,092 particles were collected for V_oND and V_oND-CaM, respectively. The datasets were normalized, bandpass-filtered, binned by 2, and circularly masked. Datasets were analyzed using reference-free alignment as implemented in EMAN2.

Twenty-seven class averages from the CaM-V_oND dataset were selected for use as initial references in a startup procedure for 3D reconstruction. Initial models were generated using the standard EMAN2 procedure and subjected to seven rounds of refinement. The resulting model was low pass-filtered to 40 Å and used to start up automated 3D refinement in Relion 1.3 (52). Half-datasets were refined independently for six iterations, and the unfiltered final maps served as inputs to the "relion_postprocess" protocol for automatic masking and a resolution estimate from calculation of the corrected gold standard Fourier shell correlation (FSC). The resolution was estimated at 14.9 Å using the 0.143 gold standard FSC cutoff (20.3 Å at 0.5 FSC). The final model was filtered to 40 Å and used as a reference for starting up the 3D reconstruction of the V_oND dataset using the Relion 1.3 autorefinement procedure as described above for the V_oND-CaM dataset. The resolution of the V_oND reconstruction was estimated at 14.9 Å using the 0.143 FSC cutoff (16.3 Å at 0.5 FSC).

Fitting of Atomic Models of Subunits—We used the atomic structure of the K_{10} ring from *E. hirae* (PDB code 2BL2) to fit into the corresponding density for the yeast V_o *c*-ring. Homology models were calculated using Phyre2 (53) for a_{NT} and subunit *d* against template bacterial subunit structures of *Meiothermus ruber* I_{NT} (PDB code 3RRK) and *Thermus thermophilus* C subunit (PDB code 1V9M). Semiautomated and manual docking of the structures was performed in Chimera (54).

Site-directed Mutagenesis of $a_{NT(1–372)}$ and Subunit d—The $a_{NT(1–372)}$ and subunit *d* constructs used in this study have been described previously (38). Site-directed mutagenesis was done using the QuikChange protocol (Stratagene). Double (R250A,K251A) and quadruple (K247A,R250,K251A, E254A) alanine mutants of $a_{NT(1–372)}$ were generated using the following primers: vph1–372-r250a-k251a-F, CTC ACG GTG ATC TGA TTA TTA AAA GAA TCG CAG CGA TTG CGG AAT CAT TGG ATG; vph1–372-r250a-k251a-R, GTA AAG ATT GGC ATC CAA TGA TTC CGC AAT CGC TGC GAT TCT TTT AAT AAT C. The quadruple mutant was generated in two steps using the double mutant as template with the following primers: vph1–372-e254a-F, CTG ATT ATT AAA AGA ATC GCA GCG ATT GCG GCA TCA TTG GAT GCC AAT C; vph1–372-e254a-R, GAT TGG CAT CGT AAA GAT TGG CAT CCA ATG ATG CCG CAA TCG CTG CGA TT; vph1–372-k247a-F, GTA TTT TCT CAC GGT GAT CTG ATT ATT GCA AGA ATC GCA GCG ATT GCG GCA TC; vph1–372-k247a-R, CAT CCA ATG ATG CCG CAA TCG CTG CGA TTC TTG CAA TAA TCA GAT CAC CGT GAG.

The triple alanine mutant construct of subunit *d* (D144A, E146A,E150A) was generated in two separate mutagenesis steps (D144A and E146A followed by E150A) using the following primers: m6-d144a-e146a-F, GTT GAG TGT TGC TAC TGC TCT TGC ATC CCT ATA CGA AAC CG; m6-d144a-e146a-R, CGG TTT CGT ATA GGG ATG CAA GAG CAG TAG CAA CAC TCA AC; m6-d144a-e146a-e150a-F, GCT CTT GCA TCC CTA TAC GCA ACC GTA TTG GTG GAT ACC; m6-d144a-e146a-e150a-R, GGT ATC CAC CAA TAC GGT TGC GTA TAG GGA TGC AAG AGC. The quadruple alanine mutant construct of subunit *d* (D37A, E40A, D41A, K43A) was generated in three sequential mutagenesis steps using the following primers: m6-a110c-F, ATA CAT CAA CTT AAC ACA ATG TGC CAC GTT GGA AGA TCT AAA ATT AC; m6–110-R, GTA ATT TTA GAT CTT CCA ACG TGG CAC ATT GTG TTA AGT TGA TGT AT; m6-a110c-a119c-a122c-F, CTT AAC ACA ATG TGC CAC GTT GGC AGC TCT AAA ATT ACA ATT ATC ATC AAC; m6-a110c-a119c-a122c-R, GTT GAT GAT AAT TGT AAT TTT AGA GCT GCC AAC GTG GCA CAT TGT GTT AAG; m6-a110c-a119c-a122c-a127g-a128c-F, CAA TGT GCC ACG TTG GCA GCT CTA GCA TTA CAA TTA TCA TCA ACT GAT TAT; m6-a110c-a119c-a122c-a127g-a128c-R, ATA ATC AGT TGA TGA TAA TTG TAA TGC TAG AGC TGC CAA CGT GGC ACA TTG. A second triple alanine mutant of subunit *d* (E198A,E199A,E202A; ITC control mutant) was generated in two steps using the following primers: M6_a593c_a596c_F, AAG ACT TTT ACA ATT TTG TCA CTG CAG CAA TTC CGG AAC CTG CTA AAG AAT G; M6_a593c_a596c_R, CAT TCT TTA GCA GGT TCC GGA ATT GCT GCA GTG ACA AAA TTG TAA AAG TCT T; M6_a605c_F, CAC TGC AGC AAT TCC GGC ACC TGC TAA AGA ATG TA; M6_a605c_R, TAC ATT CTT TAG CAG GTG CCG GAA TTG CTG CAG TG. The sequences of the $a_{NT(1–372)}$ and subunit *d* constructs were confirmed by DNA

sequencing (Eurofins) using MalE and M13 primers (New England Biolabs).

Circular Dichroism Spectroscopy—Far UV CD spectra of $a_{NT(1–372)}$ and subunit *d* constructs were collected on an Aviv 420 spectrometer in 25 mM sodium phosphate (pH 7.4) in a 1-mm path length cuvette at 10 °C. For the subunit *d* scans, 0.1 mM tris(2-carboxyethyl)phosphine (TCEP) was included in the buffer. Scans of buffer only were subtracted from the spectra.

Isothermal Titration Calorimetry—The interactions between subunit *d* and $a_{NT(1–372)}$ constructs were determined using a VP-ITC (MicroCal). Proteins were prepared in 20 mM Tris (pH 7), 0.5 mM EDTA, and 1 mM TCEP at 10 °C. Ligand (subunit *d*, 370–400 μM) was titrated into solutions of $a_{NT(1–372)}$ constructs (25 μM). The titrations were corrected for ligand heat of dilution by subtraction of blank experiments of ligand into buffer. Analysis of data was performed using MicroCal VP-ITC Origin software. After completion of the titrations, the cell contents were subjected to size exclusion chromatography over a Superdex 200 H/R 16/500 column. At least two titrations were performed for each wild type and mutant construct combinations.

Other Methods—Protein concentrations were determined using the BCA assay (Pierce) after TCA precipitation of proteins as described previously (38). Site-directed mutagenesis was verified by DNA sequencing (Eurofins).

Author Contributions—N. J. S. and S. W. designed the study. All experiments were carried out by N. J. S. N. J. S. and S. W. wrote the manuscript.

Acknowledgments—We thank Dr. Steven Ludtke for advice regarding data processing using the EMAN software package. We thank Dr. Stewart Loh for assistance with CD data collection. Sergio Couoh-Cardel is acknowledged for advice with V_o purification and Dr. Rebecca Oot and Stuti Sharma for helpful discussions.

References

1. Forgac, M. (2007) Vacuolar ATPases: rotary proton pumps in physiology and pathophysiology. *Nat. Rev. Mol. Cell Biol.* **8,** 917–929
2. Kane, P. M. (2006) The where, when, and how of organelle acidification by the yeast vacuolar H+-ATPase. *Microbiol. Mol. Biol. Rev.* **70,** 177–191
3. Marshansky, V., and Futai, M. (2008) The V-type H+-ATPase in vesicular trafficking: targeting, regulation and function. *Curr. Opin. Cell Biol.* **20,** 415–426
4. Graham, L. A., Flannery, A. R., and Stevens, T. H. (2003) Structure and assembly of the yeast V-ATPase. *J. Bioenerg. Biomembr.* **35,** 301–312
5. Zoncu, R., Bar-Peled, L., Efeyan, A., Wang, S., Sancak, Y., and Sabatini, D. M. (2011) mTORC1 senses lysosomal amino acids through an inside-out mechanism that requires the vacuolar H^+-ATPase. *Science* **334,** 678–683
6. Xu, Y., Parmar, A., Roux, E., Balbis, A., Dumas, V., Chevalier, S., and Posner, B. I. (2012) Epidermal growth factor-induced vacuolar (H+)-ATPase assembly: a role in signaling via mTORC1 activation. *J. Biol. Chem.* **287,** 26409–26422
7. Yan, Y., Denef, N., and Schüpbach, T. (2009) The vacuolar proton pump, V-ATPase, is required for notch signaling and endosomal trafficking in *Drosophila*. *Dev. Cell* **17,** 387–402
8. Sun-Wada, G. H., Toyomura, T., Murata, Y., Yamamoto, A., Futai, M., and Wada, Y. (2006) The a3 isoform of V-ATPase regulates insulin secretion from pancreatic β-cells. *J. Cell Sci.* **119,** 4531–4540
9. Vavassori, S., and Mayer, A. (2014) A new life for an old pump: V-ATPase and neurotransmitter release. *J. Cell Biol.* **205,** 7–9
10. Inoue, H., Noumi, T., Nagata, M., Murakami, H., and Kanazawa, H. (1999) Targeted disruption of the gene encoding the proteolipid subunit of mouse vacuolar H^+-ATPase leads to early embryonic lethality. *Biochim. Biophys. Acta* **1413,** 130–138
11. Smith, A. N., Skaug, J., Choate, K. A., Nayir, A., Bakkaloglu, A., Ozen, S., Hulton, S. A., Sanjad, S. A., Al-Sabban, E. A., Lifton, R. P., Scherer, S. W., and Karet, F. E. (2000) Mutations in ATP6N1B, encoding a new kidney vacuolar proton pump 116-kD subunit, cause recessive distal renal tubular acidosis with preserved hearing. *Nat. Genet.* **26,** 71–75
12. Thudium, C. S., Jensen, V. K., Karsdal, M. A., and Henriksen, K. (2012) Disruption of the V-ATPase functionality as a way to uncouple bone formation and resorption: a novel target for treatment of osteoporosis. *Curr. Protein Pept. Sci.* **13,** 141–151
13. Williamson, W. R., and Hiesinger, P. R. (2010) On the role of v-ATPase V0a1-dependent degradation in Alzheimer disease. *Commun. Integr. Biol.* **3,** 604–607
14. Brown, D., Smith, P. J., and Breton, S. (1997) Role of V-ATPase-rich cells in acidification of the male reproductive tract. *J. Exp. Biol.* **200,** 257–262
15. Karet, F. E., Finberg, K. E., Nelson, R. D., Nayir, A., Mocan, H., Sanjad, S. A., Rodriguez-Soriano, J., Santos, F., Cremers, C. W., Di Pietro, A., Hoffbrand, B. I., Winiarski, J., Bakkaloglu, A., Ozen, S., Dusunsel, R., *et al.* (1999) Mutations in the gene encoding B1 subunit of H+-ATPase cause renal tubular acidosis with sensorineural deafness. *Nat. Genet.* **21,** 84–90
16. Sennoune, S. R., Bakunts, K., Martínez, G. M., Chua-Tuan, J. L., Kebir, Y., Attaya, M. N., and Martínez-Zaguilán, R. (2004) Vacuolar H+-ATPase in human breast cancer cells with distinct metastatic potential: distribution and functional activity. *Am. J. Physiol. Cell Physiol.* **286,** C1443–C1452
17. Wong, D., Bach, H., Sun, J., Hmama, Z., and Av-Gay, Y. (2011) *Mycobacterium tuberculosis* protein tyrosine phosphatase (PtpA) excludes host vacuolar-H+-ATPase to inhibit phagosome acidification. *Proc. Natl. Acad. Sci. U.S.A.* **108,** 19371–19376
18. Xu, L., Shen, X., Bryan, A., Banga, S., Swanson, M. S., and Luo, Z. Q. (2010) Inhibition of host vacuolar H+-ATPase activity by a *Legionella pneumophila* effector. *PLoS Pathog.* **6,** e1000822
19. Kartner, N., and Manolson, M. F. (2014) Novel techniques in the development of osteoporosis drug therapy: the osteoclast ruffled-border vacuolar H^+-ATPase as an emerging target. *Expert. Opin. Drug Discov.* **9,** 505–522
20. Fais, S., De Milito, A., You, H., and Qin, W. (2007) Targeting vacuolar H+-ATPases as a new strategy against cancer. *Cancer Res.* **67,** 10627–10630
21. Bowman, E. J., and Bowman, B. J. (2005) V-ATPases as drug targets. *J. Bioenerg. Biomembr.* **37,** 431–435
22. Zhao, J., Benlekbir, S., and Rubinstein, J. L. (2015) Electron cryomicroscopy observation of rotational states in a eukaryotic V-ATPase. *Nature* **521,** 241–245
23. Powell, B., Graham, L. A., and Stevens, T. H. (2000) Molecular characterization of the yeast vacuolar H+-ATPase proton pore. *J. Biol. Chem.* **275,** 23654–23660
24. Wilkens, S. (2005) Rotary molecular motors. *Adv. Protein Chem.* **71,** 345–382
25. Muench, S. P., Trinick, J., and Harrison, M. A. (2011) Structural divergence of the rotary ATPases. *Q. Rev. Biophys.* **44,** 311–356
26. Kane, P. M. (1995) Disassembly and reassembly of the yeast vacuolar H^+-ATPase *in vivo*. *J. Biol. Chem.* **270,** 17025–17032
27. Sumner, J. P., Dow, J. A., Earley, F. G., Klein, U., Jäger, D., and Wieczorek, H. (1995) Regulation of plasma membrane V-ATPase activity by dissociation of peripheral subunits. *J. Biol. Chem.* **270,** 5649–5653
28. Kane, P. M. (2012) Targeting reversible disassembly as a mechanism of controlling V-ATPase activity. *Curr. Protein Pept. Sci.* **13,** 117–123
29. Lafourcade, C., Sobo, K., Kieffer-Jaquinod, S., Garin, J., and van der Goot, F. G. (2008) Regulation of the V-ATPase along the endocytic pathway occurs through reversible subunit association and membrane localization. *PLoS ONE* **3,** e2758
30. Sautin, Y. Y., Lu, M., Gaugler, A., Zhang, L., and Gluck, S. L. (2005) Phosphatidylinositol 3-kinase-mediated effects of glucose on vacuolar H+-ATPase assembly, translocation, and acidification of intracellular compartments in renal epithelial cells. *Mol. Cell Biol.* **25,** 575–589

31. Trombetta, E. S., Ebersold, M., Garrett, W., Pypaert, M., and Mellman, I. (2003) Activation of lysosomal function during dendritic cell maturation. *Science* **299,** 1400–1403
32. Parra, K. J., and Kane, P. M. (1998) Reversible association between the V1 and V0 domains of yeast vacuolar H+-ATPase is an unconventional glucose-induced effect. *Mol. Cell Biol.* **18,** 7064–7074
33. Delamarre, L., Pack, M., Chang, H., Mellman, I., and Trombetta, E. S. (2005) Differential lysosomal proteolysis in antigen-presenting cells determines antigen fate. *Science* **307,** 1630–1634
34. Voss, M., Vitavska, O., Walz, B., Wieczorek, H., and Baumann, O. (2007) Stimulus-induced phosphorylation of vacuolar H^+-ATPase by protein kinase A. *J. Biol. Chem.* **282,** 33735–33742
35. Parra, K. J., Keenan, K. L., and Kane, P. M. (2000) The H subunit (Vma13p) of the yeast V-ATPase inhibits the ATPase activity of cytosolic V1 complexes. *J. Biol. Chem.* **275,** 21761–21767
36. Gräf, R., Harvey, W. R., and Wieczorek, H. (1996) Purification and properties of a cytosolic V1-ATPase. *J. Biol. Chem.* **271,** 20908–20913
37. Zhang, J., Feng, Y., and Forgac, M. (1994) Proton conduction and bafilomycin binding by the V0 domain of the coated vesicle V-ATPase. *J. Biol. Chem.* **269,** 23518–23523
38. Couoh-Cardel, S., Milgrom, E., and Wilkens, S. (2015) Affinity purification and structural features of the yeast vacuolar ATPase Vo membrane sector. *J. Biol. Chem.* **290,** 27959–27971
39. Diab, H. I., and Kane, P. M. (2013) Loss of vacuolar H+-ATPase (V-ATPase) activity in yeast generates an iron deprivation signal that is moderated by induction of the peroxiredoxin TSA2. *J. Biol. Chem.* **288,** 11366–11377
40. Oot, R. A., Kane, P. M., Berry, E. A., and Wilkens, S. (2016) Crystal Structure of Yeast V1-ATPase in the Autoinhibited State. *EMBO J.* **35,** 1694–1706
41. Zhang, Z., Zheng, Y., Mazon, H., Milgrom, E., Kitagawa, N., Kish-Trier, E., Heck, A. J., Kane, P. M., and Wilkens, S. (2008) Structure of the yeast vacuolar ATPase. *J. Biol. Chem.* **283,** 35983–35995
42. Benlekbir, S., Bueler, S. A., and Rubinstein, J. L. (2012) Structure of the vacuolar-type ATPase from *Saccharomyces cerevisiae* at 11-A resolution. *Nat. Struct. Mol. Biol.* **19,** 1356–1362
43. Muench, S. P., Scheres, S. H., Huss, M., Phillips, C., Vitavska, O., Wieczorek, H., Trinick, J., and Harrison, M. A. (2014) Subunit positioning and stator filament stiffness in regulation and power transmission in the V1 motor of the *Manduca sexta* V-ATPase. *J. Mol. Biol.* **426,** 286–300
44. Wilkens, S., and Forgac, M. (2001) Three-dimensional structure of the vacuolar ATPase proton channel by electron microscopy. *J. Biol. Chem.* **276,** 44064–44068
45. Oot, R. A., Kane, P. M., Berry, E. A., and Wilkens, S. (2016) Crystal structure of yeast V1-ATPase in the autoinhibited state. *EMBO J.* **35,** 1694–1706
46. Srinivasan, S., Vyas, N. K., Baker, M. L., and Quiocho, F. A. (2011) Crystal structure of the cytoplasmic N-terminal domain of subunit I, a homolog of subunit a, of V-ATPase. *J. Mol. Biol.* **412,** 14–21
47. Murata, T., Yamato, I., Kakinuma, Y., Leslie, A. G., and Walker, J. E. (2005) Structure of the rotor of the V-Type Na+-ATPase from *Enterococcus hirae*. *Science* **308,** 654–659
48. Smardon, A. M., Nasab, N. D., Tarsio, M., Diakov, T. T., and Kane, P. M. (2015) Molecular interactions and cellular itinerary of the yeast RAVE (regulator of the H+-ATPase of vacuolar and endosomal membranes) complex. *J. Biol. Chem.* **290,** 27511–27523
49. Li, S. C., Diakov, T. T., Xu, T., Tarsio, M., Zhu, W., Couoh-Cardel, S., Weisman, L. S., and Kane, P. M. (2014) The signaling lipid PI(3,5)P(2) stabilizes V(1)-V(o) sector interactions and activates the V-ATPase. *Mol. Biol. Cell* 25, 1251–1262
50. Chung, J. H., Lester, R. L., and Dickson, R. C. (2003) Sphingolipid requirement for generation of a functional v1 component of the vacuolar ATPase. *J. Biol. Chem.* **278,** 28872–28881
51. Ritchie, T. K., Grinkova, Y. V., Bayburt, T. H., Denisov, I. G., Zolnerciks, J. K., Atkins, W. M., and Sligar, S. G. (2009) Chapter 11: reconstitution of membrane proteins in phospholipid bilayer nanodiscs. *Methods Enzymol.* **464,** 211–231
52. Scheres, S. H. (2012) RELION: implementation of a Bayesian approach to cryo-EM structure determination. *J. Struct. Biol.* **180,** 519–530
53. Kelley, L. A., Mezulis, S., Yates, C. M., Wass, M. N., and Sternberg, M. J. (2015) The Phyre2 web portal for protein modeling, prediction and analysis. *Nat. Protoc.* **10,** 845–858
54. Pettersen, E. F., Goddard, T. D., Huang, C. C., Couch, G. S., Greenblatt, D. M., Meng, E. C., and Ferrin, T. E. (2004) UCSF Chimera: a visualization system for exploratory research and analysis. *J. Comput. Chem.* **25,** 1605–1612